Multiscale Science and Engineering (2020) 2:169–188
https://doi.org/10.1007/s42493-020-00049-y

ORIGINAL RESEARCH

2D Crack Propagation in High-Strength Concrete Using Multiscale Modeling

Marcela Gimenes[1] · **Eduardo A. Rodrigues**[1] · **Michael A. Maedo**[1] · **Luís A. G. Bitencourt Jr.**[2] · **Osvaldo L. Manzoli**[1]

Received: 9 June 2020 / Revised: 11 August 2020 / Accepted: 7 September 2020 / Published online: 14 September 2020

Abstract
In this work a concurrent multiscale (macro and mesoscale) approach for high-strength concrete (HSC) is proposed for seeking to better understand the influence of coarse aggregate type, shape, and size distribution as well as the interfacial transition zone (ITZ) effects on the fracture mechanical responses. A linear elastic model with homogenized elastic properties is used for the macroscale, while a three-phase material composed of coarse aggregates, mortar matrix and the ITZ equipped with nonlinear behavior models are assumed for the mesoscopic level. To geometrically represent and gain insights into effects of coarse aggregates, two polygonal shapes are assumed: irregular quadrilateral and regular octagonal forms, which are used separated and randomly generated from a given grading curve and placed in the mesoscale region using the "take-and-place" method. A mesh fragmentation technique is used to explicitly represent the crack propagation process by considering the individual behavior of each phase as well as their mutual interactions. The non-matching macro and mesoscopic meshes are attached based on the use of coupling finite elements in the context of the rigid coupling scheme to adequately guarantee the continuity of displacement between both scales. Numerical analyses of dog-bone shape specimens under tensile load and three-point bending beams were performed. The responses obtained numerically show a good agreement with experimental ones found in literature demonstrating how the proposed approach is efficient, robust and useful for modeling crack propagation in HSC.

Keywords HSC · ITZ · Crack propagation process · Damage model · Mesh fragmentation technique · Coupling finite element

Introduction

Over the last few decades, several works have devoted to the advancement of technologies related to the increase in the concrete strength [2, 7, 31, 39]. These research efforts led to the development of high-strength concrete (HSC), in which the compressive strength of the material is higher than 50 MPa. Its performance allied to its durability have contributed to the frequent use of HSC. The difference regarding the mechanical behavior between HSC and the normal strength concrete (NSC) relies on their composition. The reaction caused by adding pozzolans (i.e., fly ash, blast furnace slag, silica fume or micro silica) to the mixture generates calcium-silicate-hydrate gel, which grants additional strength for the concrete material [34]. Currently, HSC is generally applied to the construction of bridges, deep caissons, columns of high-rise buildings, and diaphragm walls [63].

The superior compressive strength of HSC reduces its material ductility, and consequently, affects the cracking process [59]. The fact that the mortar matrix strengths are equal to or greater than the ones of the coarse aggregates contribute to an increase in brittleness [17], since in this particular case the crack may cut the aggregate interior. Therefore, nowadays, many researchers have dedicated their efforts to gain a better understanding on the mechanical behavior associated with HSC. In this context, laboratory tests have been conducted to investigate the crack formation and propagation of HSC under different loading conditions and considering various particle size

---

✉ Luís A. G. Bitencourt Jr.
luis.bitencourt@usp.br

[1] São Paulo State University-UNESP, Av. Eng. Luiz Edmundo C. Coube 14-01, Bauru, SP CEP-17033-360, Brazil

[2] Department of Structural and Geotechnical Engineering, University of São Paulo-USP, Av. Prof. Luciano Gualberto, Trav. do Biênio n. 380, São Paulo, SP CEP-05508-010, Brazil

distributions and compositions. Hussein and Marzouk [20] carried out experimental tests in four HSC plate samples and the authors discovered a dependence of concrete failure envelopes on material strength and aggregate types. Three-point bending beams were experimentally tested by Rao and Prasad [38] to determine the post peak-behavior of HSC. According to the authors, an increase in the maximum size of coarse aggregate leads to higher fracture parameters, such as fracture energy, fracture toughness and characteristic length. Wittmann [59] reported that the interaction between inclusions and cement matrix affects both fracture energy and crack initiation by means of the internal shrinkage that occurs in HSC, which induces stresses that cannot be properly reproduced by numerical simulations.

From the mesoscopic point of view, the fracturing process of HSC can be very different from the one found in traditional NSC. While in NSC the fracture propagates through the matrix, in HSC the fracture may break the coarse aggregates, since the matrix is not always the weakest phase of the composite. Consequently, the aggregate geometric characteristics and particle size distribution can also influence the macro-mechanical properties, i.e. tensile strength and fracture energy [8, 61].

The numerical simulation of cement-based materials may take place in three different levels: (i) macrolevel, which treats concrete as a homogeneous material; (ii) mesolevel, which distinguishes different constituents such as coarse aggregate, mortar matrix, interfacial transition zone (ITZ), pores and cracks; and (iii) microlevel, which refers to the microstructure of hardened cement paste [32, 58, 66]. The mesoscopic level approach in particular, is a very practicable manner to consider the heterogeneous nature of concrete. For that reason, many mesoscale models have been employed to study the mechanical behavior of concrete as a composite material using both discrete element methods, such as truss and lattice models [18, 52], and continuum finite element methods [1, 42, 56, 60].

The aggregate shape, size and distribution within the matrix may be acquired either by digital image processing [21, 32, 40, 57] or by parameterized generation [55, 56, 60]. Therefore, mesoscale models might be extremely useful in HSC numerical analysis once coarse aggregate influence can be detected, in accordance with the related experimental findings. Besides, mesoscopic models usually consider the presence of the ITZ, which may be modeled by either zero-thickness interface elements [3, 25] or standard finite elements [1, 42]. The mesolevel model might also be coupled to a macrolevel model, resulting in the so-called concurrent multiscale model [26–28, 36, 64], allowing macroscopic analysis with homogenized material properties in some parts of the domain while zooming in at specific regions for detailed mesomechanical modeling [16]. Alternatively, semi-concurrent models can also be employed based on the concept of Representative Volume Element (RVE) [48, 49].

The advent of modern computer machines led to the development of sophisticated computer techniques that admit the statistical computational design of heterogeneous composite materials [57], the improvement of nanoscale techniques to study the phenomenological behavior of nanocomposite materials [10], the explicit simulation of the interface between dissimilar materials [9, 37], as well as the internal structure of the material by considering the presence of aggregates, mortar, ITZs, as well as the voids and weak inclusions [11, 19, 55]. Such tools provide a better understanding of the concrete physical behavior. Micro and mesoscale approaches have been able to capture the main trends observed in laboratory experiments [13, 22–24, 42, 47, 65]. These numerical works showed that micro and mesoscale models are very promising to investigate how the internal components of the material affects its macroscopic structure.

It is worthwhile to mention that the representation of an entire domain in a mesoscale format is not common, specially for large scale problems. In general, the domain is divided into subdomains with different scales, so that mesh refinement is usually considered in the most critical zones. In this context, this paper employs a concurrent two-scale model to study the crack propagation process in HSC, so that coupling finite elements (CFEs) [5] are used to couple the two meshes associated with the macro and mesoscale subdomains. The macroscopic level behaves as a linear elastic material with homogenized elastic properties, while the mesoscale behavior is replicated by assuming the following three constituents: coarse aggregate, mortar matrix and ITZ. During the preprocessing stage, the mesh fragmentation technique (MFT) [30] is applied to the mesoscopic region, so that high-aspect ratio elements are introduced between the standard finite elements of the mesh. The generation and random distribution of the coarse aggregates in the mesoscale subdomain is obtained with the aid of a grading curve, following the "take-and-place" approach [60]. Moreover, homogenized properties based on a mix theory are used in the mesoscopic region to define the material parameters of each individual phase. The combination of the previous methods leads to a numerical framework capable of taking into account the aggregate effect on HSC, more specifically the effects of the coarse aggregate type, shape and size distribution, as well as the influence of the interfacial transition zone (ITZ) properties on the fracture behavior of HSC.

Multiscale Modeling of HSC

Coarse Aggregate Generation

The random generation of coarse aggregates is carried out by the use of "take-and-place" method proposed by Wriggers and Moftah [60].The aggregate particles are represented either by irregular quadrilateral or by regular octagonal geometric forms, which can be generated and placed in the mortar matrix, so that the particle sizes vary within a predetermined range. Assuming a total volume fraction of aggregate and the diameter interval, i.e. minimum ($d_{\min}$) and maximum ($d_{\max}$) allowable aggregate diameters, the aggregates can be generated following a experimental or theoretical grading curve. The theoretical Fuller and Thompson's gradation curve is a good alternative when the experimental one is not known, since it provides better compaction for aggregates [14].

From the largest to the smallest, first the aggregates are generated and, subsequently, iteratively inserted by taking into account the following two aspects: (i) the minimum distance between aggregates and the border of the sample, which is defined by the product of a defined scalar, λ_1, and the diameter of the corresponding inserted aggregate ($d_{\alpha-2}$, $d_{\alpha-1}$, d_α); (ii) the minimum distance between the aggregates itself, determined by the product of another defined scalar, λ_2, and the diameter of the actual (α) inserted aggregate, as shown in Fig. 1. Note that the iterative process is accomplished by changing the scalar values of λ_1 and λ_2, which are reduced if there is not enough space to allocate the desired volume fraction of aggregates [56].

Mesh Fragmentation Technique

The mesh fragmentation technique proposed by Manzoli et al. [30] is used as part of the multiscale strategy presented in this work, in which the HSC are represented in mesoscale by considering the following three phases: coarse aggregate, mortar matrix and the interaction region between these two phases, commonly referred to as the interfacial transition zone (ITZ) [22, 23]. Using interface elements (IEs) with high aspect ratio [29], this method enables either the properly representation of the failure behavior in the ITZ with reduced computational cost or the inherent formation and propagation of cracks that can occurs in all of these three phases of the HSC.

In previous works [41, 42], this technique was applied to simulate the normal-strength concrete in mesoscale where only the bulk finite elements (FEs) of the matrix were fragmented, since the strength of the aggregate in this case is much greater than the strength of the matrix. However, in this new strategy applied to the HSC, all bulk FEs of the mesoscopic mesh are fragmented, also allowing the free formation and propagation of cracks between the bulk elements of the aggregates.

Figure 2 summarizes the main steps related to the mesh fragmentation technique that is applied to represent the HSC in mesoscale. For the sake of simplicity, the scheme is illustrated considering only one embedded aggregate into the matrix. Thus, for a given mesoscopic geometry (Fig. 2a, e), standard three-noded triangular FEs are generated (Fig. 2b, f), followed by the fragmentation process, given by the separation of the FEs (Fig. 2c, g), and then, by inserting pairs of triangular solid FEs between all bulk elements (Fig. 2d, h) [30, 44]. It is worthwhile to comment on the thickness size of the IEs shown in (Fig. 2d, h). In this figure, the thickness of the IEs are exaggerated to make them visible. The real thickness presented in Fig. 3 and used in all the examples analyzed in this paper is set to a value of 0.01 mm, which corresponds to an approximate value of 1% of the average size of the bulk elements used. As can be seen from Fig. 3, the IEs prepared to properly represent the fracture process of each individual phase of the HSC in mesoscale are visible only if the image is zoomed in on the fragmented mesh.

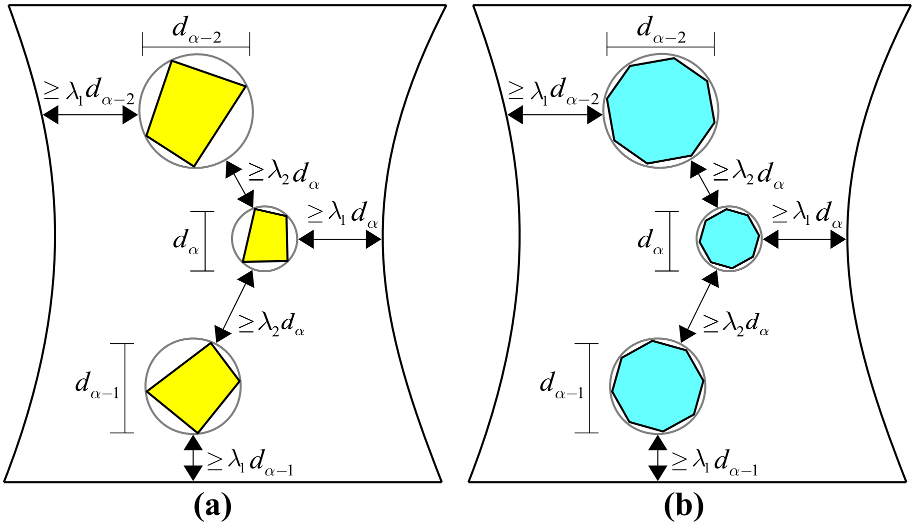

Fig. 1 Schematic illustration of the coarse aggregate "place" process for both geometries considered: **a** irregular quadrilateral and **b** regular octagonal forms

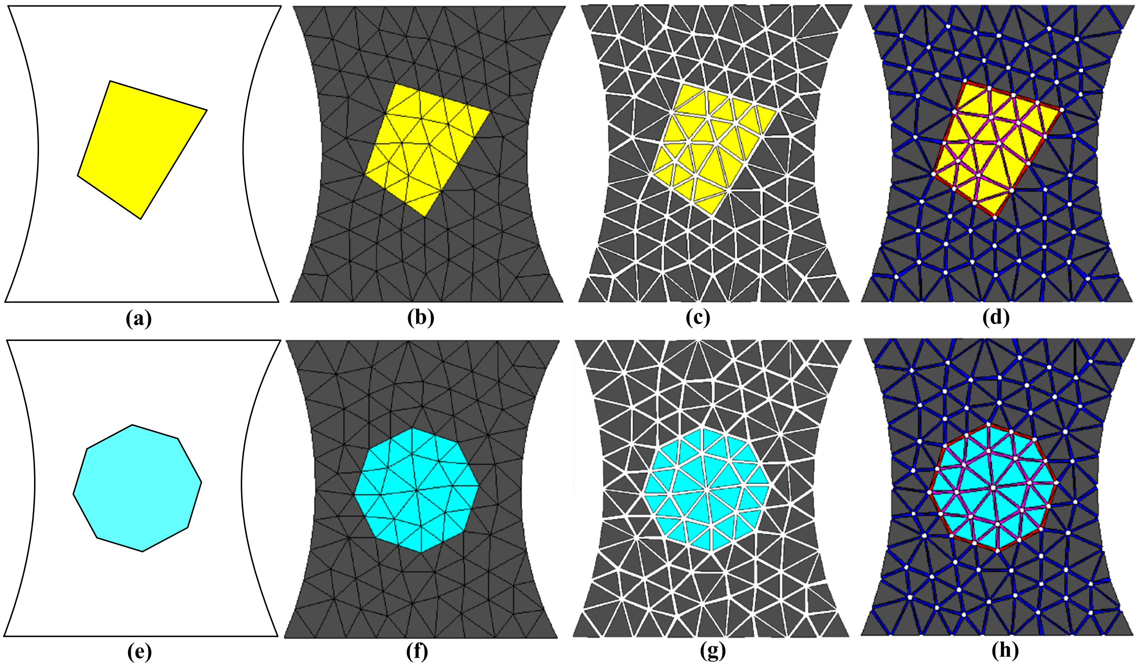

Fig. 2 Main steps of the mesh fragmentation applied to the mesoscale representation of the HSC for both aggregate geometries: **a**, **e** definition of the mesoscopic geometry, **b**, **f** generation of a standard finite element mesh, **c**, **g** separation of the standard finite elements and **d**, **h** insertion of interface finite elements

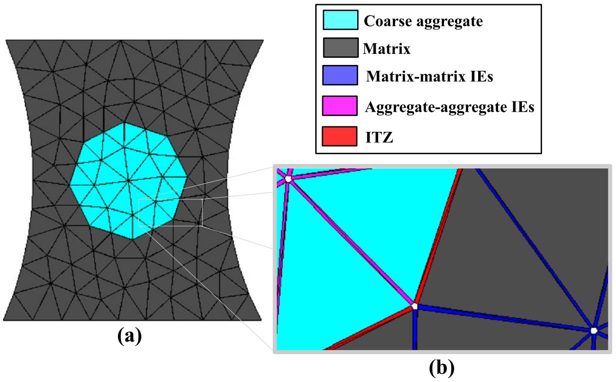

Fig. 3 Fragmented mesoscopic mesh with IEs thickness of 1% of the average size of the bulk elements: **a** conventional appearance of the fragmented mesh used in the analyses and **b** zoom of the fragmented mesh

Constitutive Damage Model

The tensile damage model proposed by Manzoli et al. [30] is used to replicate the nonlinear behavior on the IEs of each individual constituent of the HSC in mesoscale. This constitutive model was formulated and computationally implemented in the framework of implicit-explicit integration scheme (IMPL-EX) [33, 35] with a non-conventional damage criterion. The main justifications for using this model to describe the crack initiation and propagation are associated with its simplicity, ease of implementation in conventional finite element programs combined with its efficiency and robustness.

The tensile damage model briefly presented herein is formulated in the context of a single scalar damage variable defined in a closed interval that ranges from 0 to 1. The effective stress tensor computation, $\bar{\boldsymbol{\sigma}}$, from the strain tensor, $\boldsymbol{\varepsilon}$, and linear elastic tensor, $\mathbf{C}$, i.e. $\bar{\boldsymbol{\sigma}} = \mathbf{C} : \boldsymbol{\varepsilon}$, it is used as the starting point for constructing the damage model. Thus, the damage criterion is written as a function of the stress component, $\bar{\sigma}_{nn}$, obtained according to the unit vector, $\boldsymbol{n}$, normal to the IE base, i.e. $\bar{\sigma}_{nn} = \boldsymbol{n} \cdot \bar{\boldsymbol{\sigma}}\boldsymbol{n}$, as described by the following Eq. 1:

$$\bar{F}(\bar{\sigma}_{nn}, r) = \bar{\sigma}_{nn} - r \leq 0 \tag{1}$$

where r is the effective strain-like internal variable written in the space of the effective stress, which controls the size of the elastic domain.

Thus, the current stress tensor is obtained according to Eq. 2.

$$\boldsymbol{\sigma} = \begin{cases} (1-d)\bar{\boldsymbol{\sigma}} & \text{if } \bar{\sigma}_{nn} > 0 \\ \bar{\boldsymbol{\sigma}} & \text{if } \bar{\sigma}_{nn} \leq 0 \end{cases} \tag{2}$$

According to Eq. 2, the damage variable, calculated from Eq. 3, affects the effective stress tensor only if the tension stress component, $\bar{\sigma}_{nn}$, is strictly positive. Otherwise, the effective stress tensor is integrally assumed as the current stress tensor.

$$d(r) = 1 - \frac{f_t}{r} e^{Ah\left(1-\frac{r}{f_t}\right)} \tag{3}$$

It is important to observe in Eq. 3 that the damage evolution rule of the tensile damage model is expressed in terms of some important mechanical parameters, such as: the material tensile strength, f_t, the thickness of the IEs, h, and indirectly the fracture energy of the material, G_f, through the softening parameter, A, since it is obtained in terms of the fracture energy, i.e. $A = f_t^2 / EG_f$, where E is the well-known Young's modulus of the material.

In this paper only main ingredients of the tensile damage are described. More details about this model can be found in Manzoli et al. [30].

Coupling Finite Element

In order to adequately ensure the continuity of the displacement between the finite element (FE) meshes of the macro and mesoscopic scales, coupling finite elements (CFE) formulated following a rigid coupling approach are used, as proposed by Bitencourt Jr. et al. [5], This method is quite attractive, since it manages to efficiently combine non-conforming meshes, as those normally found in multiscale approaches that assumes different scale levels and, consequently, different levels of mesh refinement. In this method, the total number of degrees of freedom of the problem remains the same, which contributes significantly to the reduction of the computational cost of the problem at stake.

Figure 4 shows a schematic representation of the mesh coupling process by considering a problem where two independent subdomains (Ω_1 and Ω_2) are discretized with independent triangular FEs. Specific regular elements of the subdomain Ω_2 (called element base) with an additional node,C_{node} (i.e coupling node of the subdomain) are strategically used to couple the non-matching meshes. Such elements are called coupling finite elements (CFEs) by the authors and they have been successfully used in previous works to study the concrete material behavior [4–6, 43, 50, 51].

The CFEs can be described as standard 3-noded triangular finite elements (base elements) with an additional node (the fourth node), defined by the authors as coupling node (C_{node}) [5]. As can be seen in Fig.4, two CFEs ($\text{CFE}_1 = \{j, k, m, C_1\}$ and $\text{CFE}_2 = \{m, l, n, C_2\}$) were introduced in this illustrative example, one for each "floating node" (green nodes).

For the rigid coupling version of the CFE, the relative displacement ($[\![\mathbf{U}]\!]$), given by the difference between the displacements evaluated at point with coordinates $\mathbf{X}_C$ (defined by the position of the C_{node} that belongs to the domain of the base element) and the actual displacements of the C_{node}, shall tend to zero. So, to meet this requirement, an appropriated value needs to be adopted for the elastic constants of the matrix $\mathbf{C}$, in the definition of the reaction force ($\mathbf{F}$) associated with these relative displacements:

$$\mathbf{F}([\![\mathbf{U}]\!]) = \mathbf{C}[\![\mathbf{U}]\!] = \mathbf{C}\mathbf{B}_e\mathbf{D}_e \tag{4}$$

where $\mathbf{D}_e$ is the nodal displacement vector of the CFE and $\mathbf{B}_e$ is expressed as:

$$\mathbf{B}_e = [\overline{\mathbf{N}}_1(\mathbf{X}_c) \;\; \overline{\mathbf{N}}_2(\mathbf{X}_c) \;\; \overline{\mathbf{N}}_3(\mathbf{X}_c) \;\; -\mathbf{I}], \tag{5}$$

being $\mathbf{I}$ the identity matrix of second order, and $\overline{\mathbf{N}}_i(\mathbf{X}_c)$ is a diagonal 2×2 matrix that stores the shape functions $N_i (i = 1 : 3)$, defined by the triangular base elements.

As suggested by Bitencourt Jr. et al. [5], it was adopted $\tilde{C} = 10^9$N/mm for the elastic constants of the diagonal matrix $\mathbf{C}$:

$$\mathbf{C} = \begin{bmatrix} \tilde{C} & 0 \\ 0 & \tilde{C} \end{bmatrix}. \tag{6}$$

Therefore, the internal force vector $\mathbf{F}^{\text{int}}_{e,\Omega_{CFE}}$ and the stiffness matrix $\mathbf{K}_{e,\Omega_{CFE}}$ of a CFE can be defined as:

$$\mathbf{F}^{\text{int}}_{e,\Omega_{CFE}} = \mathbf{B}_e^T\mathbf{F}([\![\mathbf{U}]\!]) = \mathbf{B}_e^T\mathbf{C}\mathbf{B}_e\mathbf{D}_e \tag{7}$$

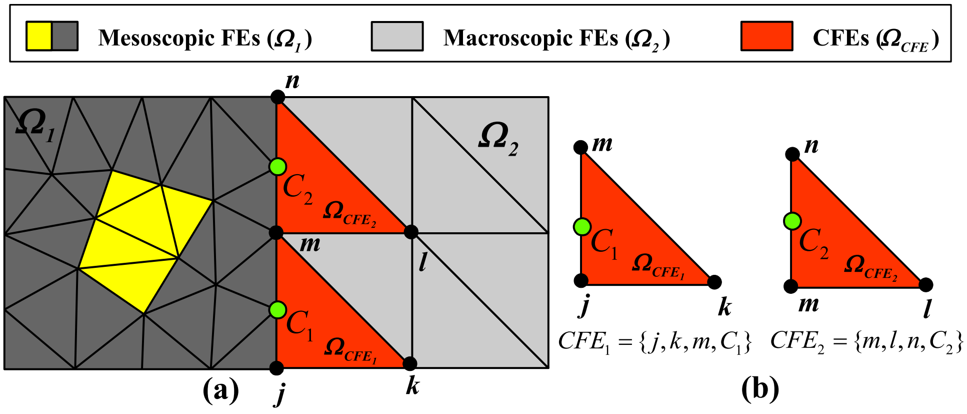

Fig. 4 Coupling finite element technique applied to the HSC multiscale model: **a** non-matching macro and mesoscopic meshes coupled via CFE and **b** details about the definition of the CFE

and

$$\mathbf{K}_{e,\Omega_{CFE}} = \frac{F^{\text{int}}_{e,\Omega_{CFE}}}{\partial \mathbf{D}_e} = \mathbf{B}_e^T \mathbf{C} \mathbf{B}_e. \tag{8}$$

Finally, the global internal force vector ($\mathbf{F}^{\text{int}}$) and the stiffness matrix ($\mathbf{K}$) can be written as:

$$\mathbf{F}^{\text{int}} = \underbrace{\mathrm{A}_{e=1}^{\text{nel}\,\Omega_1} \mathbf{F}^{\text{int}}_{e,\Omega_1}}_{\text{mesoscopic FEs}} + \underbrace{\mathrm{A}_{e=1}^{\text{nel}\,\Omega_2} \mathbf{F}^{\text{int}}_{e,\Omega_2}}_{\text{macroscopic FEs}} + \underbrace{\mathrm{A}_{e=1}^{\text{nel}\,\Omega_{CFE}} \mathbf{F}^{\text{int}}_{e,\Omega_{CFE}}}_{\text{CFEs}} \tag{9}$$

and

$$\mathbf{K} = \underbrace{\mathrm{A}_{e=1}^{\text{nel}\,\Omega_1} \mathbf{K}_{e,\Omega_1}}_{\text{mesoscopic FEs}} + \underbrace{\mathrm{A}_{e=1}^{\text{nel}\,\Omega_2} \mathbf{K}_{e,\Omega_2}}_{\text{macroscopic FEs}} + \underbrace{\mathrm{A}_{e=1}^{\text{nel}\,\Omega_{CFE}} \mathbf{K}_{e,\Omega_{CFE}}}_{\text{CFEs}} \tag{10}$$

where A stands for the finite element assembly operator. Note that the terms of these equations translates very well the use of this method in the multiscale modeling of the HSC proposed. The first term corresponds to the FEs of the mesoscopic scale, while the second term collects the information from the FEs of the macroscopic scale and, finally, the last term corresponds to the CFEs (Ω_{CFE}) used to couple both independent meshes.

It is worth mentioning that this paper only presents the main equations expressed in terms of the global coordinates system and a more detailed explanation about this technique, including the mathematical framework of CFE for non-rigid problems, can be found in Bitencourt Jr. et al. [5].

Numerical Examples

Introduction

The main objective of the numerical analyses presented herein is to obtain a better understanding of the influence of some parameters of the coarse aggregates (i.e. aggregate type, shape and grading) and the interfacial transition zone (ITZ) on the fracture behavior of HSC and, consequently, verify the accuracy and efficiency of the proposed 2D multiscale approach. For this purpose, the following three examples are numerically simulated and presented in this paper: (i) dog-bone shape specimens under tensile load, in which different fracture properties are assumed for both coarse aggregates and ITZ to investigate the influence of these parameters on the complex fracture behavior of HSC in mesoscale; (ii) notched beams with different type of coarse aggregates experimentally tested by Sengul et al. [45], which is very important to show how an improvement in the quality of the coarse aggregate can improve the tensile strength and fracture energy of the HSC and, therefore, very useful to validate the proposed approach; and (iii) three-point bending beams with different aggregate size distribution (grading curves) experimentally investigated by Siregar et al. [46]. In this third example, the ability and efficiency of the proposed model are also tested, since the sensitive responses of the fracture behavior of HSC based on its aggregate size distribution is a very challenging task.

For all the examples simulated only the homogeneous values of the elastic properties (Young's modulus and Poisson's ratio) are known, either hypothetically as in the first example or provided by the experimental data as in the last two examples. Therefore, the elastic properties of coarse aggregates are assumed and the matrix elastic properties are estimated based on the rule of mixture proposed by Counto [12].

The fracture parameters (tensile strength and fracture energy) of each phase of the composite are defined using the same strategy adopted by Rodrigues et al. [42], given by the following relation:

$$\frac{\left(X_{t_{\text{aggi}}} + X_{t_{\text{mi}}} + X_{t_{\text{itz}}}\right)}{3} = X_{t_{\text{c}}} \tag{11}$$

where $X_{t_{\text{aggi}}}$, $X_{t_{\text{mi}}}$ and $X_{t_{\text{itz}}}$ are the tensile strength or fracture energy of the aggregate, matrix and ITZ, respectively; $X_{t_{\text{c}}}$ is the tensile strength or fracture energy of the homogenized fracture properties of the composite. In addition, it is assumed that the fracture properties of the ITZ can be evaluated as a function of the fracture properties of the matrix ($X_{t_{\text{itz}}} = \hat{X}_{t_{\text{itz}}}(X_{t_{\text{mi}}})$). This relation is in accordance with experimental studies available in the literature that show that the ITZ strength is heavily influenced by the matrix strength [15, 62]. Recently, Rodrigues et al. [42] adopted a relation of $X_{t_{\text{itz}}} = 0.5X_{t_{\text{mi}}}$ for normal strength concrete. In this work, it is assumed that the fracture properties of the ITZ correspond to 70% of the fracture properties of the matrix ($X_{t_{\text{itz}}} = 0.7X_{t_{\text{mi}}}$), which is in accordance with the interval values (50% and 70%) reported by Giaccio et al. [17] and Chen and Liu [8] for high-strength concrete.

Dog-Bone Specimen

In this first example a dog-bone shape specimen is numerically simulated to understand the influence of the mesoscopic constituents on the mechanical behavior of high-strength concrete (HSC). For this purpose, two polygonal shapes (i.e., irregular quadrilateral and regular octagonal) are used to represent the coarse aggregates. The main difference between the two shapes is the high angularity of the irregular aggregates configuration. Using these two aggregate shapes separately, a parametric study of the HSC is performed in mesoscale by varying the aggregate tensile strength and, subsequently, the fracture properties (tensile strength and fracture energy) of the ITZ. Such numerical experiments can be used to assess how these parameters affect the crack pattern and the structural responses. The main motivation for carrying out these studies (i.e., choosing two different geometries to represent the coarse aggregates) is based on results of previous works reported in the literature which indicate that the type and shape of the coarse aggregates and the interaction that occurs between aggregates and mortar matrix (ITZ) can significantly affect the fracture behavior of both normal and high-strength concrete [22, 45, 61]. Furthermore, the level of influence of each of these parameters is directly related to the target strength of the concrete and the quality of the aggregate used [45].

For the reference HSC studied, the following homogenized properties are adopted: Young's modulus of 46.0 GPa, Poisson's ratio of 0.2, tensile strength of 5.0 MPa and fracture energy of 0.122 N/mm. For the coarse aggregate the Young's modulus of 50.0 GPa and Poisson's ratio of 0.2 are assumed. Thus, the calculated Young's modulus of 45.0 GPa and Poisson's ratio of 0.2 are used for the matrix.

For this study, the dog-bone with out of plane thickness of 100 mm has its region of interest, i.e. the potential failure region, represented in mesoscale. The coarse aggregates are randomly generated and placed one-by-one into the matrix, assuming the Fuller's grading curve distribution, with a constant volume fraction of 40% and aggregate diameter size that varies from 4 to 8 mm. In plane stress condition, the analyses are carried out by imposing the boundary conditions illustrated in Fig. 5. It is important to mention that the geometry assumed for the dog-bone numerically studied in this paper is the same experimentally investigated by van Vliet and van Mier [53] for conventional concrete. In Fig. 5a it is possible to note the typically FE mesh used to discretize the dog-bone with either irregular or octagonal aggregates. It is also possible to observe details about the interface elements used in the mesh fragmentation process, described in Sect. 2.2, which are properly used to represent the nonlinear behavior of the two mains components of the composite (coarse aggregate and mortar matrix), as well as the complex behavior of the ITZ between them (see Fig.5b). On average, 23,500 three-node triangular FEs are used to discretize the mesoscopic level. Observe that the extreme parts of the dog-bone domain, in which the failure is not expected, is represented in macroscale with homogenized elastic properties and discretized with a coarse mesh composed of 16

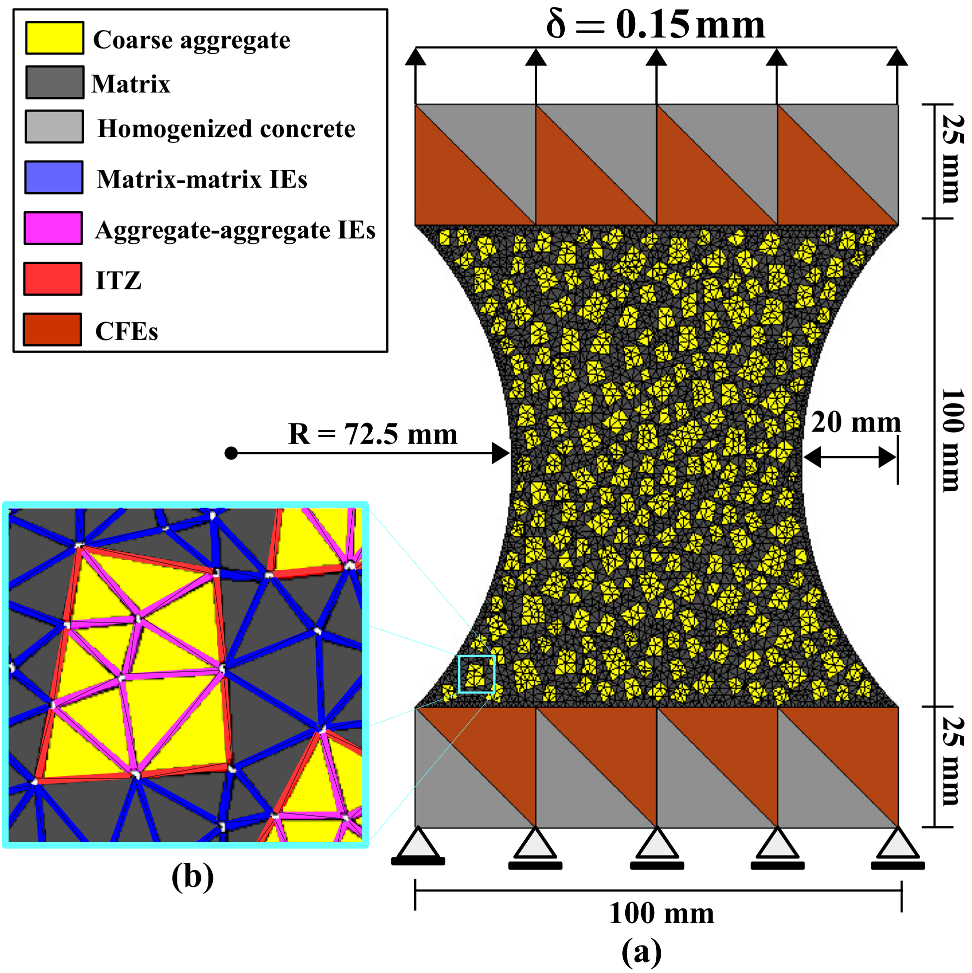

Fig. 5 Dog-bone: **a** geometry, boundary conditions, the macro and mesoscopic FE meshes used and **b** details about the fragmented mesh

triangular FEs. This scheme brings many advantages to the finite element model: it facilitates the application of boundary conditions, reduces the computational cost and also avoids any local numerical instability. Thus, on average, 150 CFEs are employed to couple both non-matching macro and mesoscopic meshes. All the analyses are carried out applying a total displacement of 0.15 mm in 1500 load steps of 1.0×10^{-4} mm.

The Coarse Aggregate Tensile Strength Effect

Table 1 shows the fracture properties assumed for the proposed study. Keeping the fracture properties of the matrix-matrix and ITZ interface elements constant, the analyses are performed by varying only the tensile strength of the coarse aggregate. Figure 6 illustrates the very tortuous crack path obtained, which in general showed to be highly dependent either on the tensile strength or the shape of aggregates. For both aggregate shapes, it is possible to note the aggregate breakage predominance for the two weakest aggregates tensile strength (see Fig. 6a, b, d, e). On the other hand, in cases where aggregates are more resistant (Fig. 6c, f) the ITZ becomes the weakest link of the composite, with the predominance of the crack passing round (ITZ failure). These statements can be quantitatively confirmed by the ratio between the predominant fracture length of each individual phase in the mesoscale and the predominant total fracture length shown in Table 2. As can be observed in this table, for aggregates with tensile strengths of $f_{t_{aggi}} = 3.0\,\text{MPa}$ and $f_{t_{aggi}} = 4.0\,\text{MPa}$, the respective percentage fracture lengths obtained by the aggregate breakage for both aggregate shapes are: 59.27% and 79.20%, 37.88% and 77.48%. For the tensile strength value of $f_{t_{aggi}} = 5.0\,\text{MPa}$, the respective percentage fracture lengths obtained by the ITZ failure for both aggregate shapes are: 45.61% and 56.12% of the total fracture lengths.

Figure 7 shows the deformed configurations of the samples at an initial stage of fracture propagation that occurs in the load step 160 with a high scaling factor of 1, 500 times the original shape. It is worth noting how well the initial cracks are distributed, especially for the case involving the weakest irregular aggregate (see Fig. 7a). In this case, the initial cracks start at the aggregates, even those that are relatively distant from the central region of high stress concentration in the specimen. Some of these cracks continue to spread towards the mortar, culminating in a dominant macro-crack formation, as illustrated in details in Fig. 8. In this figure, the following load steps and scaling factors are adopted: load step 150 with a scaling factor of 2500 (Fig. 8a, b), load step 180 with a scaling factor of 1000 (Fig. 8c) and load step 210 with a scaling factor of 600 times the original configuration (Fig. 8d). Figure 9 shows the principal stress for the specimen yet in the elastic regime (load step 60) for both irregular and octagonal aggregate shapes.

Table 1 Fracture properties used to study the aggregate tensile strength effects

Phase	Tensile strength (MPa)	Fracture energy (N/mm)
Aggregate–aggregate interface	$f_{t_{aggi}} = 3.0$	$G_{f_{aggi}} = 0.100$
	$f_{t_{aggi}} = 4.0$	$G_{f_{aggi}} = 0.100$
	$f_{t_{aggi}} = 5.0$	$G_{f_{aggi}} = 0.100$
Matrix–matrix interface	$f_{t_{mi}} = 6.0$	$G_{f_{mi}} = 0.158$
ITZ	$f_{t_{itz}} = 4.2$	$G_{f_{itz}} = 0.111$

The influence of aggregates on the crack propagation are reflected in the quantitative structural responses obtained in terms of load vs. displacement shown in Fig. 10. The weaker aggregate contributes negatively to the dog-bone's tensile strength for both aggregate shapes. As shown in Fig. 11, the geometric shape of the aggregates has a significant effect on HSC performance only for the weakest aggregates (poor aggregates) (see Fig. 11a), while minor effects are observed as the tensile strength of the aggregate approaches the tensile strength of the mortar matrix, indicating that the appropriate selection of aggregates (high-quality aggregates) can improve the tensile strength of the HSC. Furthermore, the multiscale strategy proposed can capture well the aggregate effects on the HSC.

The ITZ Fracture Properties Effect

Herein the influence analysis of four different ITZ fracture properties on the fracture behavior of HSC is presented. The fracture properties assumed are listed in Table 3. From the qualitative results obtained is possible to neatly note that the main crack pattern is highly influenced by the two smallest fracture properties assumed for the ITZ, either for the irregular aggregates illustrated in Fig. 12a, b or for the octagonal (regular) aggregates shown in Fig. 13a, b. As the fracture properties of the aggregates are kept constant and, as the properties of the ITZ tend to the properties of the matrix, the crack patterns become very similar for the two aggregate shapes, as illustrated in Fig. 12c, d and in Fig. 13c, d, respectively. This can be explained by the fact that the aggregates become the weakest phase of the composite and, consequently, the crack propagation breaking through aggregates are predominant, as can be demonstrated quantitatively by the percentages of fracture lengths described in Table 4.

The quantitative results obtained in terms of load vs. displacement for both aggregate shapes are shown in Fig. 14. It is important to note how the poor quality of ITZ properties can drastically reduce the tensile strength

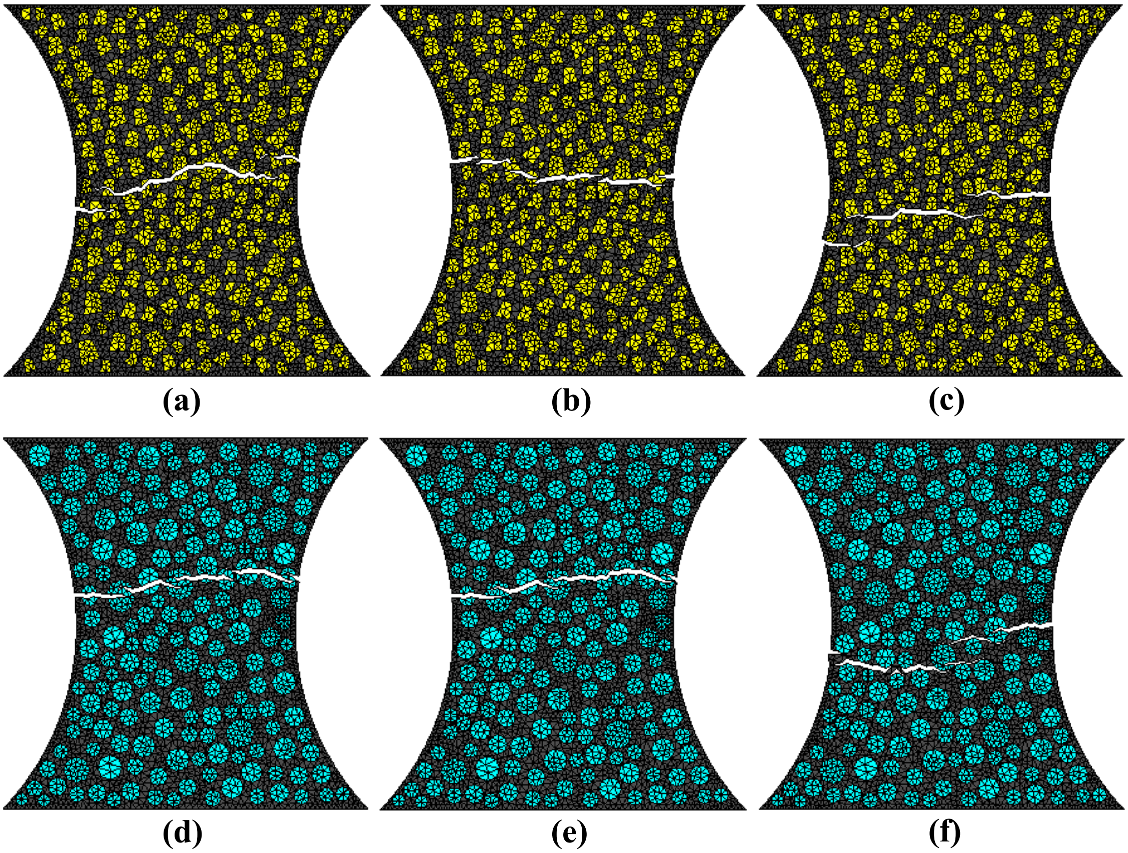

Fig. 6 Dog-bone: final crack patterns obtained for both aggregate shapes with different tensile strength: **a**, **d** 3.0 MPa, **b**, **e** 4.0 MPa and **c**, **f** 5.0 MPa (scaling factor of 10)

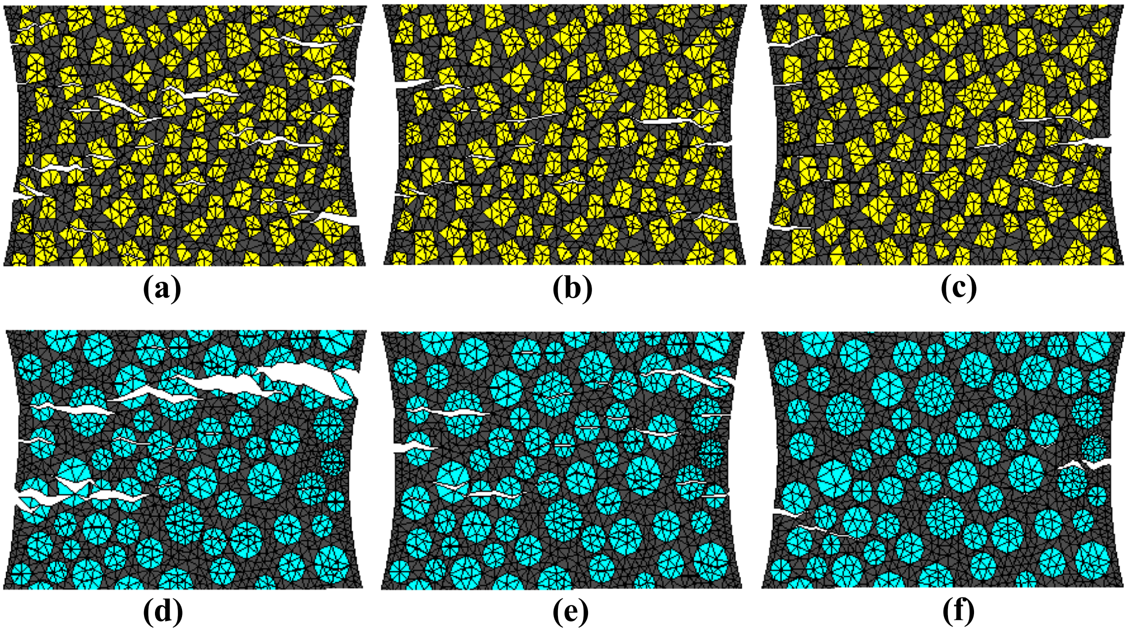

Fig. 7 Dog-bone: initial crack patterns obtained for the step-load 160 for both aggregate shapes with different tensile strength: **a**, **d** 3.0 MPa, **b**, **e** 4.0 MPa and **c**, **f** 5.0 MPa (scaling factor of 1500)

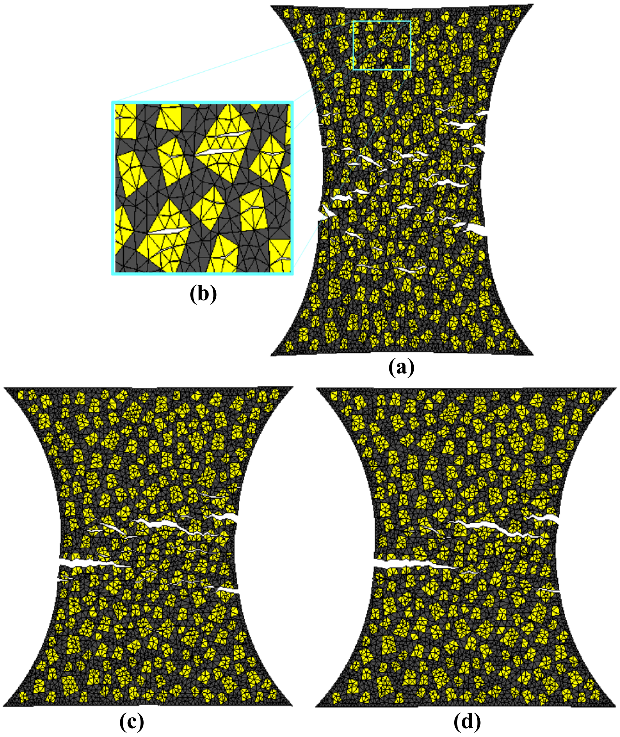

Fig. 8 Dog-bone: details about the crack initiation, propagation and coalescence obtained for the weakest irregular aggregate: **a**, **b** step-load 150 (scaling factor of 1500), **c** step-load 180 (scaling factor of 1000) and **d** step-load 210 (scaling factor of 600)

of the dog-bone for both irregular and octagonal aggregate shapes (see Fig. 14a, b for IA and OA—ITZ-3 MPa). On the other hand, neither the tensile strength nor the fracture energy are sharply affected by the coarse aggregate shapes, as illustrated in Fig. 15a–d.

Due to the low quantitative responses obtained for the weakest fracture properties assumed for ITZ, it can be stated that this important phase of the HSC requires special attention. Furthermore, the responses obtained for the ITZ with enhanced fracture properties indicate that the quality of the HSC can be significantly improved with the improvement of the ITZ properties.

Notched Beam with Different Coarse Aggregate Types

In this second example the three-point bending beams experimentally investigated by Sengul et al. [45] are numerically simulated. Seeking to better understand the influence of the coarse aggregate type on the mechanical behavior of high-strength concrete (HSC), the authors developed a series of tests using notched beams under bending load. The concrete mixtures used basalt, sandstone, eocene and devonian crushed limestone as coarse aggregates.

In the numerical analysis proposed in this section, only the beams with eocene and devonian crushed limestone coarse aggregates are simulated. The main reason for choosing these two rocks is associated with the relative high quality on the mechanical properties of the devonian limestone (DL) compared to the eocene limestone (EL). Figure 16 shows the details about the geometry of the beam, the FE meshes and boundary conditions assumed. Using the method described in Sect. 2.1, the coarse aggregates are generated and placed randomly within the central region of beam, assuming a constant volume fraction of 40%, and the minimum and maximum aggregate diameter size of $d_{\min} = 6\,\text{mm}$ and $d_{\max} = 30\,\text{mm}$, respectively, as reported in the experimental data. Due to the relative small influence provided by the two different aggregate shapes observed in the previous example, only the more regular octagonal geometric forms will be used henceforth to represent the coarse aggregate embedded into the matrix.

From the experimental parameters (homogenized parameters) of the HSC, i.e. Young's modulus, concrete tensile strength and fracture energy, and the crushed limestone properties provided by the authors [45], the numerical parameters adopted for the concrete in macroscale and for the different phases in mesoscale are listed in Table 5. To discretize both the macro and mesoscale a structured mesh

Fig. 9 Dog-bone: principal stress obtained for the step-load 60 for the weakest aggregate tensile strength

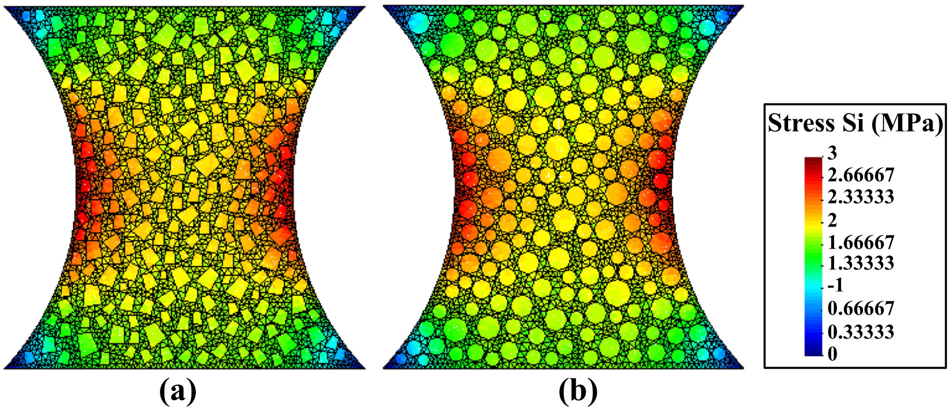

Table 2 Percentage of each phase of the HSC intercepted by the main fracture for distinct aggregate tensile strengths

Coarse aggregate shapes	Aggregate tensile strength (MPa)	Matrix–matrix IEs (%)	Aggregate–aggregate IEs (%)	ITZ (%)
Irregular	$f_{t_{aggi}} = 3.0$	30.09	59.27	10.64
	$f_{t_{aggi}} = 4.0$	34.37	37.88	27.75
	$f_{t_{aggi}} = 5.0$	31.49	22.89	45.61
Regular	$f_{t_{aggi}} = 3.0$	18.89	79.20	1.91
	$f_{t_{aggi}} = 4.0$	19.57	77.48	2.95
	$f_{t_{aggi}} = 5.0$	31.35	12.52	56.12

with 512 triangular FEs and an unstructured mesh composed, on average, of 9500 FEs are respectively used. In addition, on average 70 FEs are strategically used to couple the non-matching meshes.

In plane stress condition with out of plane thickness of 100 mm, the analyses are carried out applying a total of 2000 load steps, while the crack mouth opening displacement (CMOD) is controlled, in which an opening of 2.0×10^{-4} mm is imposed per each load step. Figure 17 shows the deformed configuration of the central part of the simulated beam, in which a greater tendency of the crack to pass through (cut) the EL than the DL aggregates is observed, since the EL coarse aggregates are the weakest phase of the composite.

The numerical results obtained in terms of load vs. CMOD agrees very well with the experimental responses either for the HSC with devonian or eocene limestones, as illustrated in Fig. 18. In Fig. 19, it is possible to note the high influence provided by the coarse aggregate type on the structural responses. It is worth noting how the aggregates quality can improve both the tensile strength and the fracture energy. In addition, the comparison of the results from

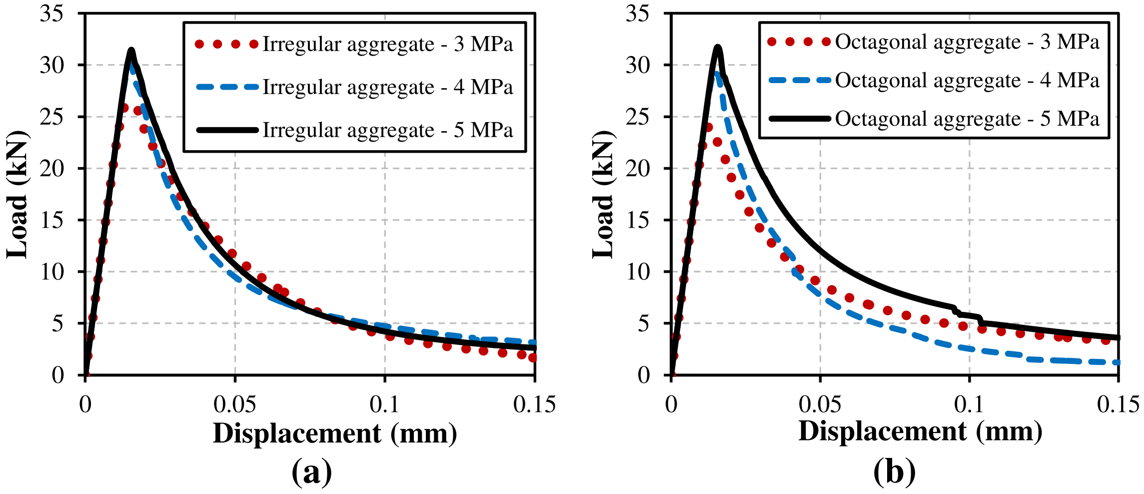

Fig. 10 Dog-bone: load-displacement curves obtained for both shapes: **a** irregular aggregates (IA) and **b** octagonal aggregates (OA)

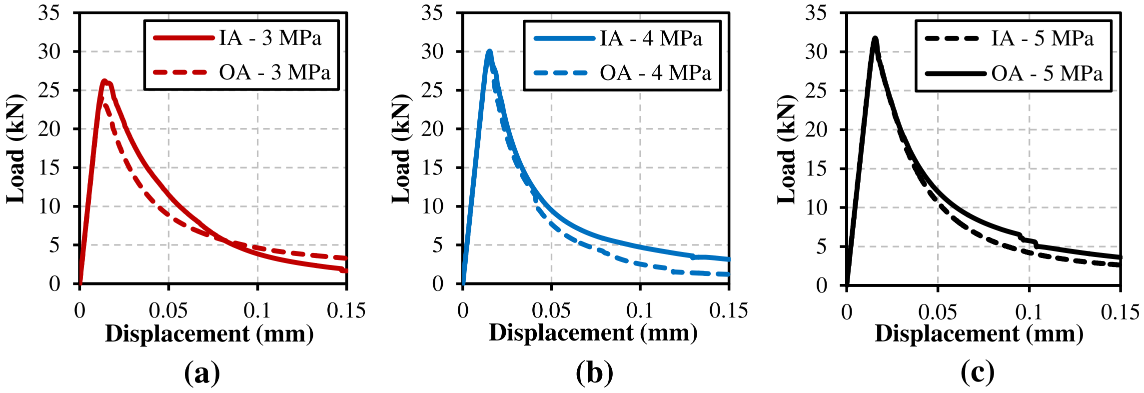

Fig. 11 Dog-bone: load-displacement curves for the two aggregate shapes (IA and OA) obtained for the different tensile strength: **a** 3.0 MPa, 4.0 MPa and 5.0 MPa

Table 3 Fracture properties used to study the ITZ effects

Phase	Tensile strength (MPa)	Fracture energy (N/mm)
Aggregate–aggregate interface	$f_{t_{aggi}} = 4.5$	$G_{f_{aggi}} = 0.100$
Matrix–matrix interface	$f_{t_{mi}} = 6.0$	$G_{f_{mi}} = 0.158$
ITZ	$f_{t_{itz}} = 3.0$	$G_{f_{itz}} = 0.079$
	$f_{t_{itz}} = 4.5$	$G_{f_{itz}} = 0.118$
	$f_{t_{itz}} = 5.5$	$G_{f_{itz}} = 0.145$
	$f_{t_{itz}} = 6.0$	$G_{f_{itz}} = 0.158$

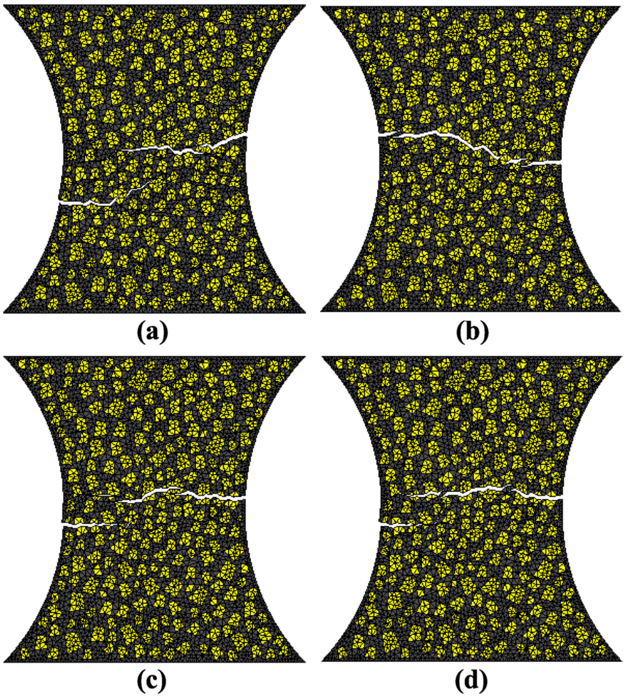

Fig. 12 Dog-bone: final crack patterns obtained for the irregular aggregate shape with the respectively tensile strength and fracture energy: **a** 3.0 MPa and 0.079 N/mm; **b** 4.5 MPa and 0.118 N/mm; **c** 5.5 MPa and 0.145 N/mm; **d** 5.5 MPa and 0.158 N/mm (scaling factor of 10)

numerical simulations and laboratory tests shows the ability of the proposed model to capture all main phenomena associated with cracking process in HSC.

Three-Point Bending Beams

In this last example some of the notched beams experimentally tested by Siregar et al. [46] are numerically analyzed to assess the capacity of proposed multiscale approach in represent the crack propagation process in mode I, taking into account the inherent failure behavior of the mesoscopic level of the HSC. In their work, the authors conducted three-point bending tests in beams with the same size to investigate the influence of different aggregate size distributions on the fracture behavior of HSC. For each case, they measured the crack mouth opening displacement (CMOD) and deflection. The beams have length of 850 mm, support mid-span of 800 mm, cross-sectional area of 100 mm × 100 mm and notch with depth and width of 25 mm and 2.5 mm, respectively.

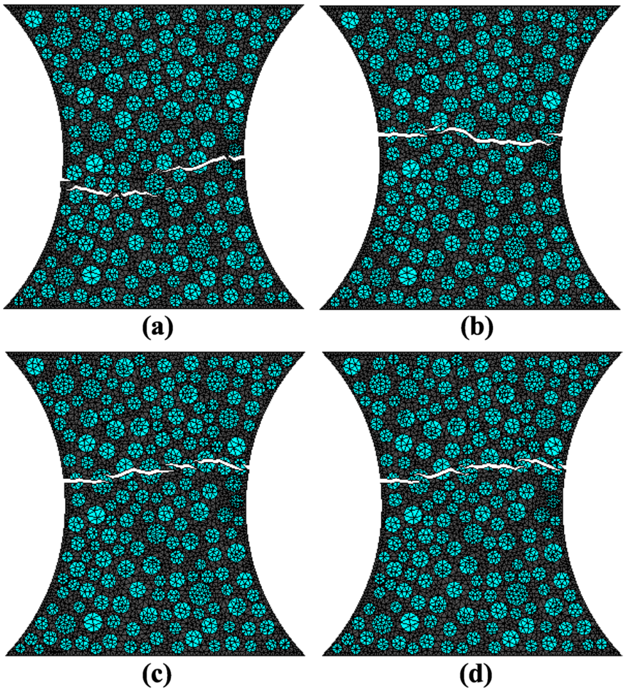

Fig. 13 Dog-bone: final crack patterns obtained for the octagonal aggregate shape with the respectively tensile strength and fracture energy: **a** 3.0 MPa and 0.079 N/mm; **b** 4.5 MPa and 0.118 N/mm; **c** 5.5 MPa and 0.145 N/mm; **d** 6.0 MPa and 0.158 N/mm (scaling factor of 10)

In the numerical analysis, only the experimental beams prepared in accordance with the first concrete mixture (i.e. the highest strength concrete) and the two aggregate distributions (grading curves 1 and 2) within the range of 5–16, as illustrated in Fig. 20, are simulated. Fig. 21 illustrates the multiscale discretization of the beam that, as in the previously developed examples, the coarse aggregates (volume fraction of 40%) are generated and placed only in the region near of the notch and, consequently, a fine fragmented mesh is considered in that region in order to adequately represent the nonlinear behavior of the different phases of the HSC in mesoscale. For each grading curve shown in Fig. 20, three numerical analyses are performed, considering three different realizations of coarse aggregates. The material properties adopted for homogenized HSC and for each constituent of the mesoscale models are listed in Table 6.

Table 4 Percentage of each phase of the HSC intercepted by the main fracture for distinct ITZ fracture properties

Coarse aggregate shapes	ITZ tensile strength (MPa) and fracture energy (N/mm)	Matrix–matrix IEs (%)	Aggregate–aggregate IEs (%)	ITZ (%)
Irregular	$f_{t_{\mathrm{itz}}} = 3.0$ and $G_{f_{\mathrm{itz}}} = 0.079$	28.83	17.38	53.79
	$f_{t_{\mathrm{itz}}} = 4.5$ and $G_{f_{\mathrm{itz}}} = 0.118$	33.29	38.33	28.38
	$f_{t_{\mathrm{itz}}} = 5.5$ and $G_{f_{\mathrm{itz}}} = 0.145$	37.29	50.82	11.89
	$f_{t_{\mathrm{itz}}} = 6.0$ and $G_{f_{\mathrm{itz}}} = 0.158$	45.50	44.80	9.70
Regular	$f_{t_{\mathrm{itz}}} = 3.0$ and $G_{f_{\mathrm{itz}}} = 0.079$	34.37	9.82	55.81
	$f_{t_{\mathrm{itz}}} = 4.5$ and $G_{f_{\mathrm{itz}}} = 0.118$	33.26	51.82	14.93
	$f_{t_{\mathrm{itz}}} = 5.5$ and $G_{f_{\mathrm{itz}}} = 0.145$	29.33	66.82	3.85
	$f_{t_{\mathrm{itz}}} = 6.0$ and $G_{f_{\mathrm{itz}}} = 0.158$	20.49	78.08	1.43

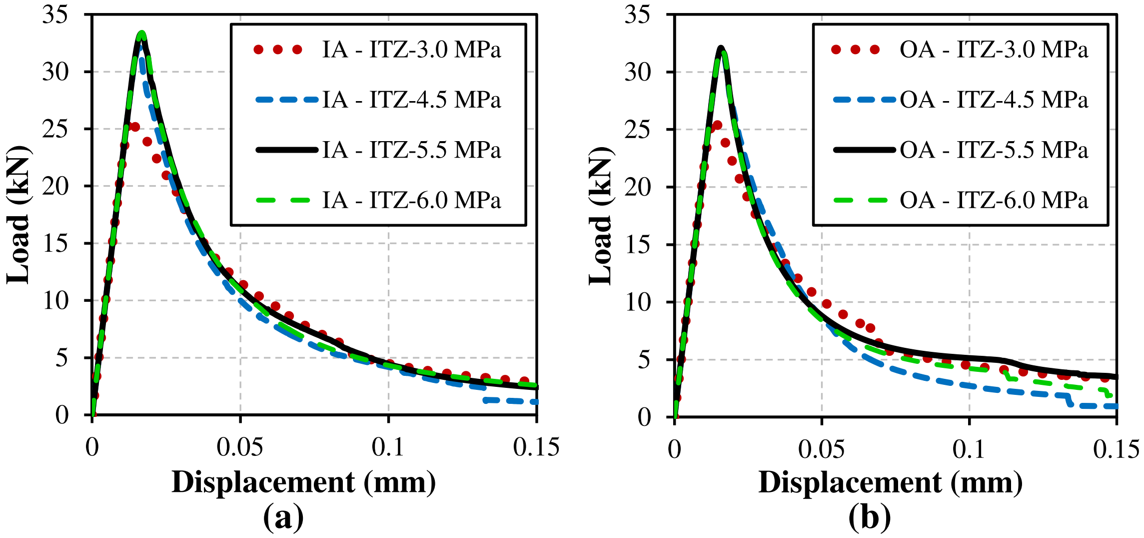

(a)

(b)

Fig. 14 Dog-bone: load-displacement curves obtained for different ITZ fractures properties for both shapes: **a** irregular aggregates (IA) and **b** octagonal aggregates (OA)

The deformed shape of the beams with the tortuous crack path associated with the coarseness properties of the aggregates are illustrated in Fig. 22. Figure 22a, c, e shows the crack patterns for the first grading curve (grading curve 1), while the predominant final crack patterns for the second grading curve (grading curve 2) are shown in Fig. 22b, d, f.

Figure 23 compares the predicted applied load vs. CMOD obtained with the numerical simulations against the experimental results reported by Siregar et al. [46]. It is possible to note that for both numerical curves the peak-load and the softening regime slightly overestimate the experimental responses. However, it is worth to noting how the proposed approach is able to reproduce the effect of the aggregate size distribution on the fractures behavior of HSC, which presents a higher peak-load for the second grading curve, in accordance with the experimental results.

Conclusions

A concurrent multiscale approach aimed to numerically simulate the effect of the coarse aggregate type, shape and size distribution, as well as the influence of the interfacial transition zone (ITZ) properties on the fracture behavior of

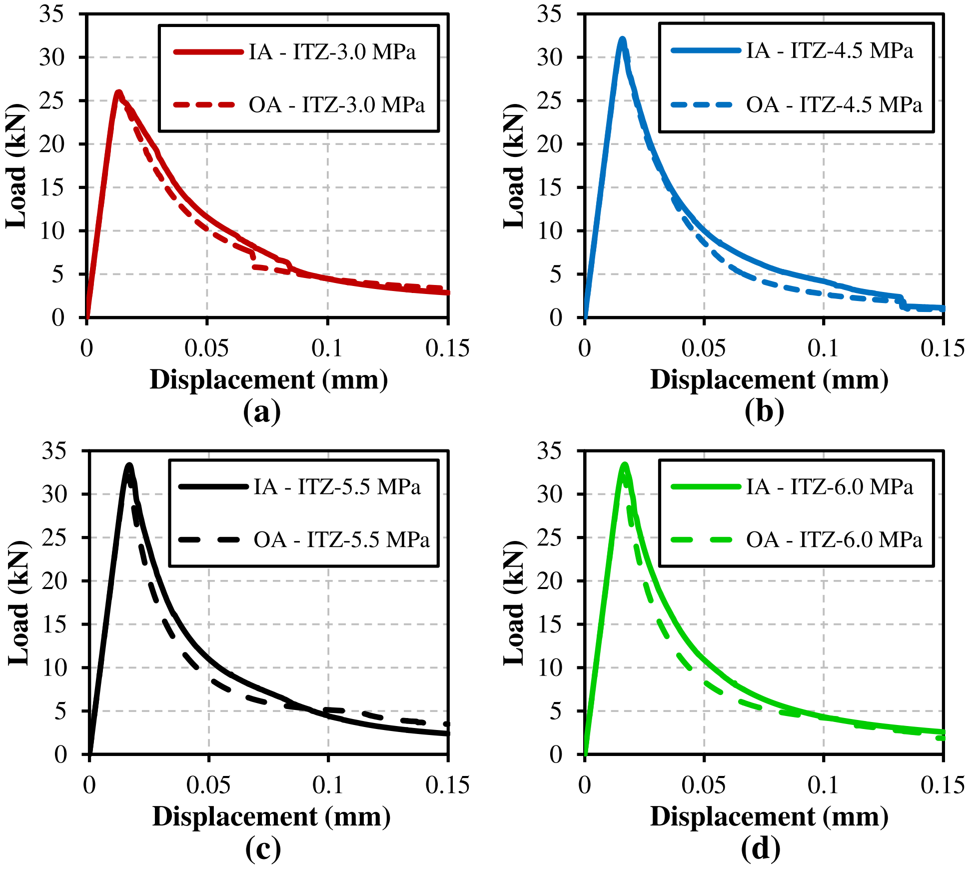

Fig. 15 Dog-bone: load-displacement curves for the two aggregate shapes (IA and OA) obtained for different tensile strength and fracture energy: **a** 3.0 MPa and 0.079 N/mm; **b** 4.5 MPa and 0.118 N/mm; **c** 5.5 MPa and 0.145 N/mm; **d** 6.0 MPa and 0.158 N/mm

Table 5 Material parameters for the HSC beams with eocene and devonian limestone coarse aggregates

Materials	Young's modulus (GPa)	Poisson's ratio	Fracture energy (N/mm)	Tensile strength (MPa)
HSC: Eocene Limestone (EL)				
Concrete	$E_c = 39.60$	$\nu_c = 0.2$	–	–
Devonian limestone (EL)	$E_{EL} = 21.50$	$\nu_{EL} = 0.2$	-	-
Matrix	$E_m = 55.50$	$\nu_m = 0.2$	–	–
Matrix–matrix interface	$E_{mi} = 55.50$	$\nu_{mi} = 0$	$G_{f_{mi}} = 0.10$	$f_{t_{mi}} = 7.5$
EL–EL interface	$E_{ELi} = 21.50$	$\nu_{ELi} = 0$	$G_{f_{ELi}} = 0.07$	$f_{t_{ELi}} = 3.0$
ITZ	$E_{itz} = 55.50$	$\nu_{itz} = 0$	$G_{f_{itz}} = 0.07$	$f_{t_{itz}} = 5.25$
HSC: Devonian Limestone (DL)				
Concrete	$E_c = 48.10$	$\nu_c = 0.2$	–	–
Devonian limestone (DL)	$E_{EL} = 40.00$	$\nu_{EL} = 0.2$	–	–
Matrix	$E_m = 55.50$	$\nu_m = 0.2$	–	–
Matrix–matrix interface	$E_{mi} = 55.50$	$\nu_{mi} = 0$	$G_{f_{mi}} = 0.10$	$f_{t_{mi}} = 7.50$
DL–DL interface	$E_{DLi} = 40.00$	$\nu_{DLi} = 0$	$G_{f_{DLi}} = 0.17$	$f_{t_{DLi}} = 6.45$
ITZ	$E_{itz} = 55.50$	$\nu_{itz} = 0$	$G_{f_{itz}} = 0.07$	$f_{t_{itz}} = 5.25$

high-strength concrete (HSC) was proposed. For this purpose, a three-phase mesoscale material modeling of HSC was presented, where two polygonal geometric forms, irregular quadrilateral that presents high angularities and more rounded (octagonal) shapes, were considered to study the effects of the aggregate shape on the mechanical responses. Using the "take and place" method proposed by Wriggers and Moftah [60] these aggregates were

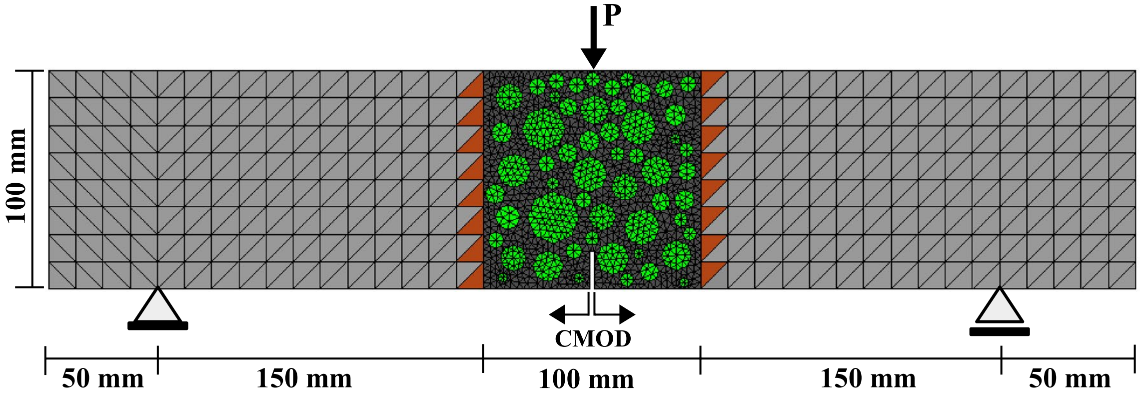

Fig. 16 Notched beam: geometry, boundary conditions and the macro and mesoscopic FE meshes adopted

Fig. 17 Notched beam: deformed shape of the beams for two coarse aggregate realizations for HSC with: **a**, **b** devonian limestone and **c**, **d** eocene limestone crushed aggregates (scaling factor of 20)

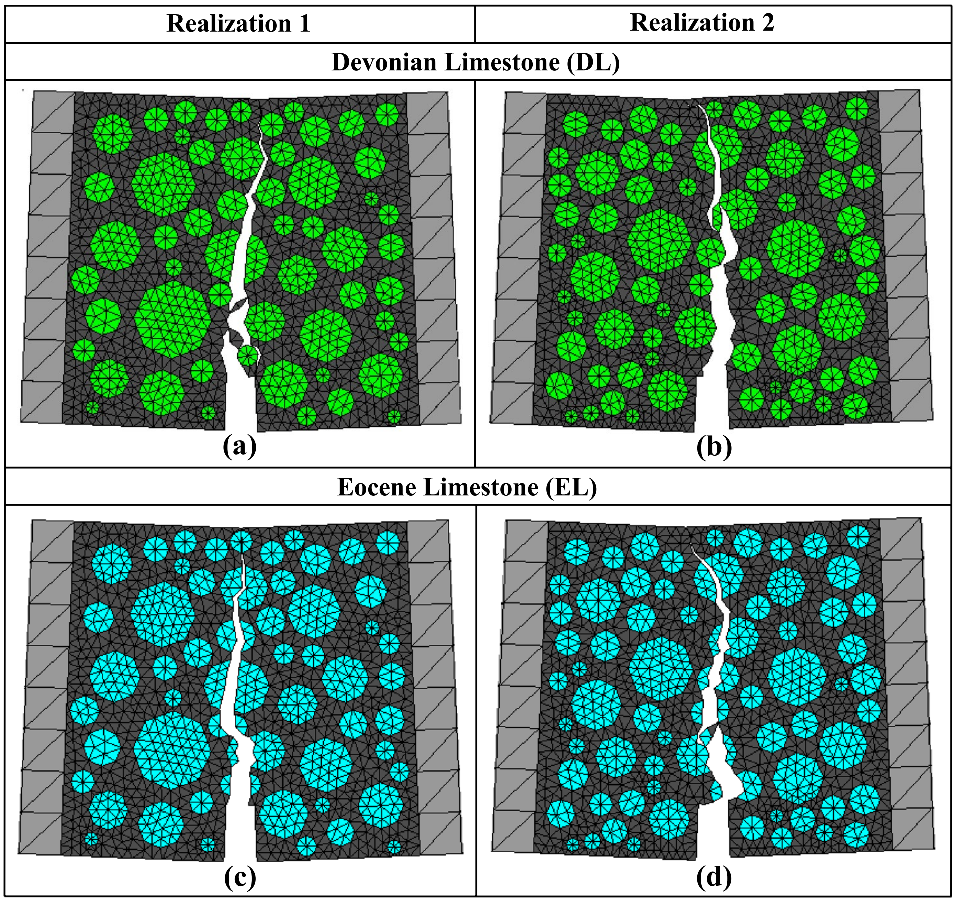

separated, randomly generated and properly embedded into the mortar matrix. In addition, to explicitly represent the crack propagation process in each mesoscopic constituents, the mesh fragmentation technique that is based on the use of interface element (IE) with high aspect ratio equipped with an effective and robust tensile damage model were used [30]. Some advantages of the strategy proposed for the HSC in mesoscale can be highlighted herein: (i) the complex crack initiation in the weakest phase followed by its propagation and coalescence were accurately captured; (ii) fracture properties of the ITZ

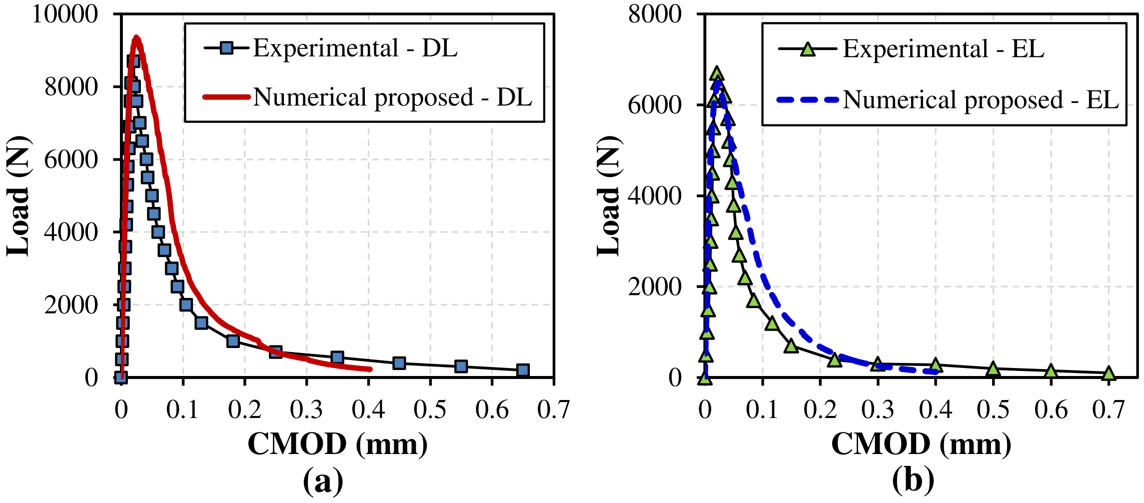

Fig. 18 Notched beam: numerical applied load vs. crack mouth opening displacement (CMOD) obtained for: **a** devonian and **b** eocene limestone coarse aggregates compared with those obtained experimentally by Sengul et al. [45]

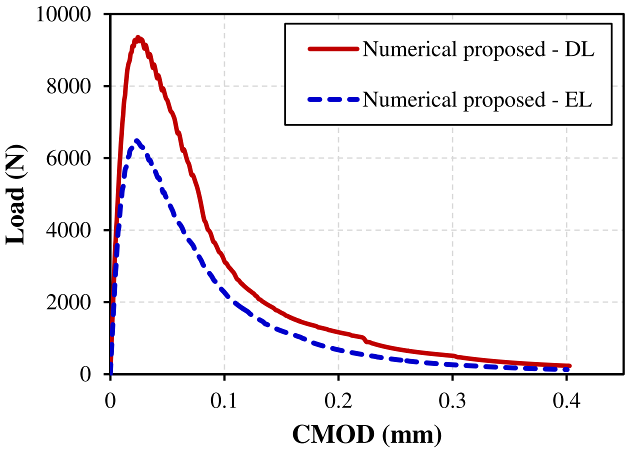

Fig. 19 Notched beam: applied load vs. CMOD for HSC with devonian and eocene limestone coarse aggregates

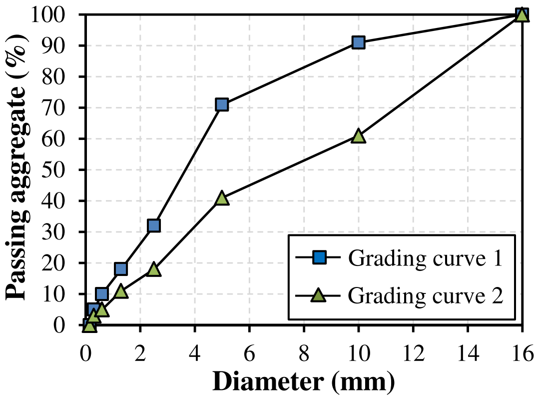

Fig. 20 Experimental aggregate grading curves provided by Siregar et al. [46]

and its consequently effects on the HSC fracture behavior could be explicitly included into the analyses without drastically increasing the total number of finite elements for that; (iii) no special scheme to track the crack paths during the analysis were needed; (iv) the methods are formulated integrally in the framework of the continuum mechanics; and (v) with the tensile damage model formulated in the context of the IMPL-EX resources [33, 35], which robustly ensures convergence even for the complex crack propagation process observed in the analyses.

Regarding the concurrent multiscale proposed in this paper, the main objective was to reduce the computational cost involved in the analyses. Thus, whenever possible, the majority of the domain of the problems were represented on a macroscale, assuming a linear elastic model set with homogenized elastic properties. In addition, the efficient coupling element technique formulated in the framework of the rigid coupling, as proposed by Bitencourt Jr. et al. [5] was applied to couple the non-matching macro and mesoscopic meshes and, therefore, guarantee the correct continuity of displacement between both scale. This technique has a very important advantage, since the conventional system of finite element equations remains the same, since this technique does not require the addition of new degrees of freedom.

In order to study and validate the proposed framework, firstly dog-bone shape specimens subjected to tensile load were simulated, at first varying the type of aggregates and, later, varying the fracture properties of the ITZ, using the two aggregate shapes proposed. The results showed that

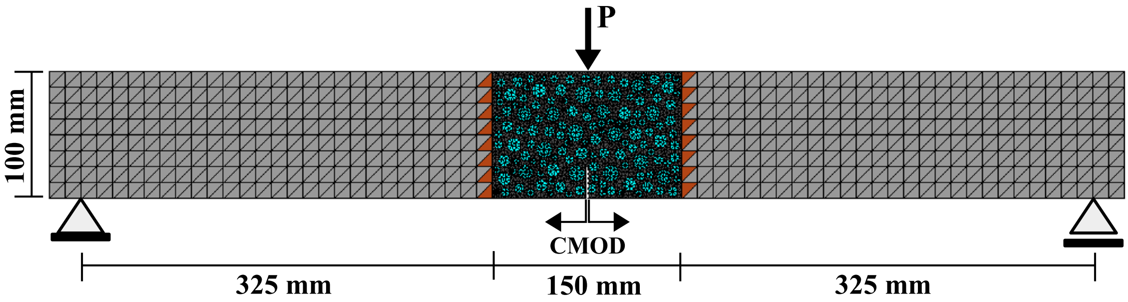

Fig. 21 Bending beam: geometry, boundary conditions and FE mesh adopted

Table 6 Material parameters for the HSC beams with different grading curves

Materials	Young's modulus (GPa)	Poisson's ratio	Fracture energy (N/mm)	Tensile strength (MPa)
Concrete	$E_c = 51.00$	$\nu_c = 0.2$	–	–
Aggregate	$E_{agg} = 50.00$	$\nu_{agg} = 0.2$	–	–
Matrix	$E_m = 51.70$	$\nu_m = 0.2$	–	–
Matrix–matrix interface	$E_{mi} = 51.70$	$\nu_{mi} = 0$	$G_{f_{mi}} = 0.158$	$f_{t_{mi}} = 6.0$
Aggregate–aggregate interface	$E_{aggi} = 50.00$	$\nu_{aggi} = 0$	$G_{f_{aggi}} = 0.100$	$f_{t_{aggi}} = 4.0$
ITZ	$E_{itz} = 51.70$	$\nu_{itz} = 0$	$G_{f_{itz}} = 0.111$	$f_{t_{itz}} = 4.2$

both aggregate types and ITZ significantly affect the HSC fracture behavior in mesoscale, in accordance with literature references [8, 17, 54]. In an inadequate situation where low-quality aggregates are used, the crack propagation breaking through the aggregates are predominant culminating in a very tortuous predominant crack, since the coarse aggregates are the weakest phase of the composite, which contributes negatively to the ultimate tensile strength of the specimen. On the other hand, when high-quality aggregates are employed, the ITZ becomes the weakest link and the debond (passing round) between aggregates and matrix predominates, leading to a consequent decrease in ultimate tensile strength. However, the results obtained for different aggregate shapes had been found to have little effect on the quantitative results, such as the tensile strength and fracture energy.

In the second example, notched beams with two types of coarse aggregates (i.e., eocene or devonian crushed limestone coarse aggregates) experimentally investigated by Sengul et al. [45] were simulated. Both the qualitative and the quantitative numerical results showed to be very sensitive to the aggregate type, indicating that the quality of the aggregates can improve either the tensile strength or the fracture energy, which agrees very well with the experimental responses obtained by Sengul et al. [45], which validated the proposed approach.

Lastly, three-point bending beams with different aggregate size distribution experimentally tested by Siregar et al. [46] were also simulated. It is worthwhile to comment on the capacity of the proposed multiscale approach in properly capturing the very sensitive and complex aggregate size distribution effects on the quantitative HSC fracture behavior, reinforcing the validation and also showing how the proposed framework is efficient and robust. In a future paper, the authors intend to extend the methodology for 3D simulations, which can be more physically representative.

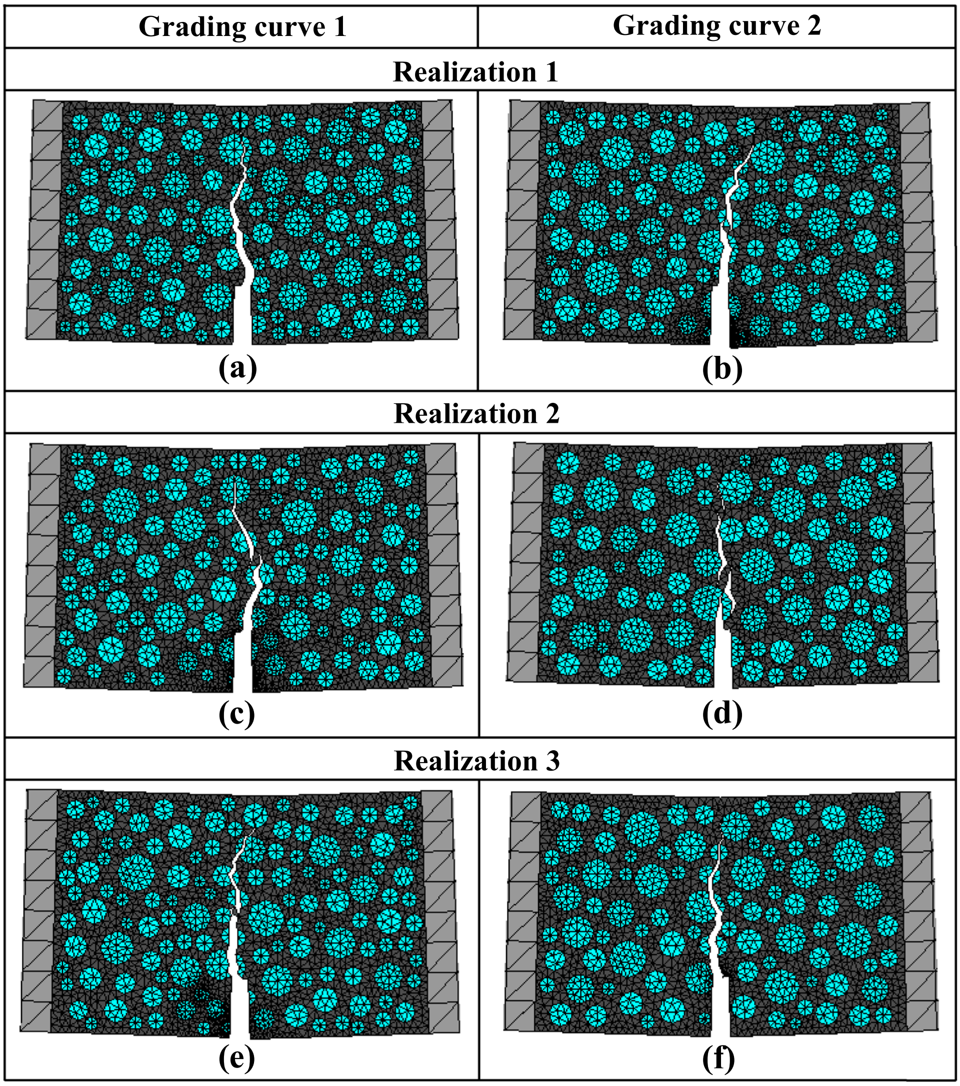

Fig. 22 Bending beam: deformed configuration of the beams for three coarse aggregate realizations for the: **a**, **c**, **d** grading curve 1 and **b**, **d**, **f** grading curve 2 (scaling factor of 10)

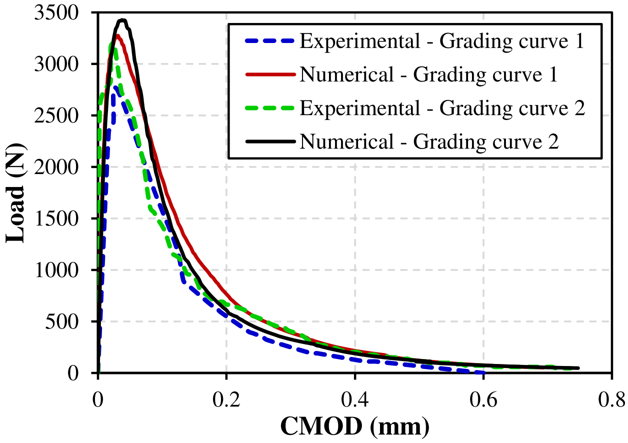

Fig. 23 Bending beam: numerical response obtained in terms of applied load vs. CMOD for the two grading curves compared against the experimental results obtained by Siregar et al. [46]

Acknowledgements The authors wish to acknowledge the financial support of the National Council for Scientific and Technological Development (CNPq) (Proc.: 423379/2016-0 and 310401/2019-4), Coordination for the Improvement of Higher Education Personnel (CAPES) and São Paulo Research Foundation (FAPESP) (Proc.: 2018/05784-3).

References

1. Z. Agioutantis, E. Chatzopoulou, M. Stavroulaki, A numerical investigation of the effect of the interfacial zone in concrete mixtures under uniaxial compression: the case of the dilute limit. Cement Concrete Res. **30**(5), 715–723 (2000)
2. P.-C. Aïtcin, P.K. Mehta, Effect of coarse aggregate characteristics on mechanical properties of high-strength concrete. Mater. J. **87**(2), 103–107 (1990)
3. M.F. Benedetto, A. Caggiano, G. Etse, Virtual elements and zero thickness interface-based approach for fracture analysis of heterogeneous materials. Comput. Methods Appl. Mech. Eng. **338**, 41–67 (2018)

4. L.A.G. Bitencourt Jr., O.L. Manzoli, T.N. Bittencourt, F.J. Vecchio, Numerical modeling of steel fiber reinforced concrete with a discrete and explicit representation of steel fibers. Int. J. Solids Struct. **159**, 171–190 (2019). https://doi.org/10.1016/j.ijsolstr.2018.09.028
5. L.A.G. Bitencourt Jr., O.L. Manzoli, P.G.C. Prazeres, E.A. Rodrigues, T.N. Bittencourt, A coupling technique for non-matching finite element meshes. Comput. Methods Appl. Mech. Eng. **290**, 19–44 (2015)
6. L.A.G. Bitencourt Jr., O.L. Manzoli, Y.T. Trindade, E.A. Rodrigues, D. Dias-da-Costa, Modeling reinforced concrete structures using coupling finite elements for discrete representation of reinforcements. Finite Elem. Anal. Des. **149**, 32–44 (2018). https://doi.org/10.1016/j.finel.2018.06.004
7. M.A. Caldarone, *High-strength concrete: a practical guide* (CRC Press, Boca Raton, 2008)
8. B. Chen, J. Liu, Effect of aggregate on the fracture behavior of high strength concrete. Constr. Build. Mater. **18**(8), 585–590 (2004)
9. Y.-H. Choi, H.-G. Kim, Development of a cohesive zone model for fatigue crack growth. Multiscale Sci. Eng. **13**, 42–53 (2020)
10. I. Chung, M. Cho, Recent studies on the multiscale analysis of polymer nanocomposites. Multiscale Sci. Eng. **1**, 167–195 (2019)
11. S.-Y. Chung, J.-S. Kim, T.-S. Han, Effects of void clustering on the thermal and mechanical properties of concrete evaluated using numerical methods. Multiscale Sci. Eng. **1**(3), 196–209 (2019)
12. U.J. Counto, The effect of the elastic modulus of the aggregate on the elastic modulus, creep and creep recovery of concrete. Mag. Concrete Res. **16**(48), 129–138 (1964)
13. J. Eliáš, M. Vořechovskỳ, Fracture in random quasibrittle media: I. discrete mesoscale simulations of load capacity and fracture process zone. Eng. Fract. Mech. **235**, 107160 (2020)
14. W. B. Fuller, S. E. Thompson, The laws of proportioning concrete (1907)
15. Y. Gao, G. De Schutter, G. Ye, Z. Tan, K. Wu, The ITZ microstructure, thickness and porosity in blended cementitious composite: effects of curing age, water to binder ratio and aggregate content. Compos. B Eng. **60**, 1–13 (2014)
16. S. Ghosh, Adaptive concurrent multi-level model for multiscale analysis of composite materials including damage, *Multiscale modeling and simulation of composite materials and structures* (Springer, Berlin, 2008), pp. 83–163
17. G. Giaccio, C. Rocco, D. Violini, J. Zappitelli, R. Zerbino, High-strength concretes incorporating different coarse aggregates. Mater. J. **89**(3), 242–246 (1992)
18. P. Grassl, D. Grégoire, L.R. Solano, G. Pijaudier-Cabot, Meso-scale modelling of the size effect on the fracture process zone of concrete. Int. J. Solids Struct. **49**(13), 1818–1827 (2012)
19. Y. Huang, Z. Yang, X. Chen, G. Liu, Monte carlo simulations of meso-scale dynamic compressive behavior of concrete based on x-ray computed tomography images. Int. J. Impact Eng. **97**, 102–115 (2016)
20. A. Hussein, H. Marzouk, Behavior of high-strength concrete under biaxial stresses. ACI Mater. J. **97**(1), 27–36 (2000)
21. A.P. Jivkov, D.L. Engelberg, R. Stein, M. Petkovski, Pore space and brittle damage evolution in concrete. Eng. Fract. Mech. **110**, 378–395 (2013)
22. M. Königsberger, B. Pichler, C. Hellmich, Micromechanics of ITZ—aggregate interaction in concrete Part I: stress concentration. J. Am. Ceram. Soc. **97**(2), 535–542 (2014a)
23. M. Königsberger, B. Pichler, C. Hellmich, Micromechanics of ITZ—aggregate interaction in concrete Part II: strength upscaling. J. Am. Ceram. Soc. **97**(2), 543–551 (2014b)
24. M. Königsberger, B. Pichler, C. Hellmich, Multiscale poro-elasticity of densifying calcium-silicate hydrates in cement paste: an experimentally validated continuum micromechanics approach. Int. J. Eng. Sci. **147**, 103196 (2020)
25. A. Kwan, Z. Wang, H. Chan, Mesoscopic study of concrete II: nonlinear finite element analysis. Comput. Struct. **70**(5), 545–556 (1999)
26. O. Lloberas-Valls, D. Rixen, A. Simone, L. Sluys, Domain decomposition techniques for the efficient modeling of brittle heterogeneous materials. Comput. Methods Appl. Mech. Eng. **200**(13), 1577–1590 (2011)
27. O. Lloberas-Valls, D. Rixen, A. Simone, L. Sluys, Multiscale domain decomposition analysis of quasi-brittle heterogeneous materials. Int. J. Numer. Meth. Eng. **89**(11), 1337–1366 (2012a)
28. O. Lloberas-Valls, D. Rixen, A. Simone, L. Sluys, On micro-to-macro connections in domain decomposition multiscale methods. Comput. Methods Appl. Mech. Eng. **225–228**, 177–196 (2012b)
29. O. Manzoli, A. Gamino, E. Rodrigues, G. Claro, Modeling of interfaces in two-dimensional problems using solid finite elements with high aspect ratio. Comput. Struct. **94–95**, 70–82 (2012)
30. O.L. Manzoli, M.A. Maedo, L.A.G. Bitencourt, E.A. Rodrigues, On the use of finite elements with a high aspect ratio for modeling cracks in quasi-brittle materials. Eng. Fract. Mech. **153**, 151–170 (2016)
31. P. Mehta, P. Monteiro, *Concrete: microstructure, properties, and materials* (McGraw-Hill, New York, 2013)
32. M. Nitka, J. Tejchman, Meso-mechanical modelling of damage in concrete using discrete element method with porous ITZs of defined width around aggregates. Eng. Fract. Mech. 107029 (2020)
33. J. Oliver, A. Huespe, J. Cante, An implicit/explicit integration scheme to increase computability of non-linear material and contact/friction problems. Comput. Methods Appl. Mech. Eng. **197**(21—-24), 1865–1889 (2008)
34. C. Poon, L. Lam, Y. Wong, A study on high strength concrete prepared with large volumes of low calcium fly ash. Cem. Concr. Res. **30**(3), 447–455 (2000)
35. P.G.C. Prazeres, L.A.G. Bitencourt Jr., T.N. Bittencourt, O.L. Manzoli, A modified implicit-explicit integration scheme: an application to elastoplasticity problems. J. Braz. Soc. Mech. Sci. Eng. (2015). https://doi.org/10.1007/s40430-015-0343-3
36. Z. Qian, E. Schlangen, G. Ye, K. Van Breugel, Modeling framework for fracture in multiscale cement-based material structures. Materials **10**(6), 587 (2017)
37. R. Qin, D. Lau, Evaluation of the moisture effect on the material interface using multiscale modeling. Multiscale Sci. Eng. **1**(2), 108–118 (2019)
38. G.A. Rao, B.R. Prasad, Fracture energy and softening behavior of high-strength concrete. Cem. Concr. Res. **32**(2), 247–252 (2002)
39. A. Ravitheja, G. Pavan Kumar, C. Madhu Anjaneyulu, Impact on cementitious materials on high strength concrete—a review. Materials Today: Proceedings (2020).
40. W. Ren, Z. Yang, P. Withers, Meso-scale fracture modelling of concrete based on x-ray computed tomography images. In: The 5th Asia-Pacific congress on computational mechanics (APCOM). Singapore (2013)
41. E.A. Rodrigues, O.L. Manzoli, L.A.G. Bitencourt Jr., 3D concurrent multiscale model for crack propagation in concrete. Comput. Methods Appl. Mech. Eng. **361**, 112813 (2020)
42. E.A. Rodrigues, O.L. Manzoli, L.A.G. Bitencourt Jr., T.N. Bittencourt, 2D mesoscale model for concrete based on the use of interface element with a high aspect ratio. Int. J. Solids Struct. **94**, 112–124 (2016)
43. E.A. Rodrigues, O.L. Manzoli, L.A.G. Bitencourt Jr., T.N. Bittencourt, M. Sánchez, An adaptive concurrent multiscale model

for concrete based on coupling finite elements. Comput. Methods Appl. Mech. Eng. **328**, 26–46 (2018)

44. M. Sánchez, O. Manzoli, L. Guimarães, Modeling 3-D desiccation soil crack networks using a mesh fragmentation technique. Comput. Geotechnics **62**, 27–39 (2014)
45. O. Sengul, C. Sengul, G. Keskin, Y. Akkaya, C. Tasdemir, M. A. Tasdemir, Fracture and microstructural studies on normal and high strength concretes with different types of aggregates. In: 8th International Conference on Fracture Mechanics of Concrete and Concrete Structures, FraMCoS-8, Toledo–Spain (2013)
46. A. Siregar, M.I. Rafiq, M. Mulheron, Experimental investigation of the effects of aggregate size distribution on the fracture behaviour of high strength concrete. Constr. Build. Mater. **150**, 252–259 (2017)
47. P. Thilakarathna, K. K. Baduge, P. Mendis, V. Vimonsatit, H. Lee, Mesoscale modelling of concrete–a review of geometry generation, placing algorithms, constitutive relations and applications. Eng. Fract. Mech. 106974 (2020)
48. S. Toro, P.J. Sánchez, P.J. Blanco, E. de Souza Neto, A.E. Huespe, R. Feijóo, Multiscale formulation for material failure accounting for cohesive cracks at the macro and micro scales. Int. J. Plast. **76**, 75–110 (2016)
49. S. Toro, P.J. Sánchez, A.E. Huespe, S.M. Giusti, P.J. Blanco, R. Feijóo, A two-scale failure model for heterogeneous materials: numerical implementation based on the finite element method. Int. J. Numer. Meth. Eng. **97**(5), 313–351 (2014)
50. Y.T. Trindade, L.A.G. Bitencourt Jr., O.L. Manzoli, Design of SFRC members aided by a multiscale model: Part II - Predicting the behavior of RC-SFRC beams. Compos. Struct. **241**, 112079 (2020a)
51. Y.T. Trindade, L.A.G. Bitencourt Jr., R. Monte, A.D. de Figueiredo, O.L. Manzoli, Design of SFRC members aided by a multiscale model: part I–predicting the post-cracking parameters. Compos. Struct. **241**, 112078 (2020b)
52. J. van Mier, M. van Vliet, Influence of microstructure of concrete on size/scale effects in tensile fracture, size-scale effects. Eng. Fract. Mech. **70**(16), 2281–2306 (2003)
53. M.R. van Vliet, J.G. van Mier, Experimental investigation of size effect in concrete and sandstone under uniaxial tension. Eng. Fract. Mech. **65**(2–3), 165–188 (2000)
54. K. Vishalakshi, V. Revathi, S.S. Reddy, Effect of type of coarse aggregate on the strength properties and fracture energy of normal and high strength concrete. Eng. Fract. Mech. **194**, 52–60 (2018)
55. X. Wang, Z. Yang, A.P. Jivkov, Monte Carlo simulations of mesoscale fracture of concrete with random aggregates and pores: a size effect study. Construct. Build. Mater. **80**, 262–272 (2015)
56. Z. Wang, A. Kwan, H. Chan, Mesoscopic study of concrete i: generation of random aggregate structure and finite element mesh. Comput. Struct. **70**(5), 533–544 (1999)
57. Y. Wei, D.H. Olsen, C.M. Miller, K.B. Wagner, A. Keyhani, N. Thadhani, M. Zhou, Computational design of three-dimensional multi-constituent material microstructure sets with prescribed statistical constituent and geometric attributes. Multiscale Sci. Eng. 1–13 (2020)
58. F. Wittmann, Structure of concrete with respect to crack formation. Fract. Mech. Concrete **43**(5), 6 (1983)
59. F. Wittmann, Crack formation and fracture energy of normal and high strength concrete. Sadhana **27**(4), 413–423 (2002)
60. P. Wriggers, S. Moftah, Mesoscale models for concrete: Homogenisation and damage behaviour. Finite Elem. Anal. Des. **42**(7), 623–636 (2006), the Seventeenth Annual Robert J. Melosh Competition. The Seventeenth Annual Robert J. Melosh Competition
61. K.-R. Wu, B. Chen, W. Yao, D. Zhang, Effect of coarse aggregate type on mechanical properties of high-performance concrete. Cem. Concr. Res. **31**(10), 1421–1425 (2001)
62. Y. Xie, D.J. Corr, F. Jin, H. Zhou, S.P. Shah, Experimental study of the interfacial transition zone (ITZ) of model rock-filled concrete (RFC). Cement Concr. Compos. **55**, 223–231 (2015)
63. H. Yazıcı, The effect of curing conditions on compressive strength of ultra high strength concrete with high volume mineral admixtures. Build. Environ. **42**(5), 2083–2089 (2007)
64. J. Zhang, X. Liu, Y. Yuan, H. Mang, Multiscale modeling of the effect of the interfacial transition zone on the modulus of elasticity of fiber-reinforced fine concrete. Comput. Mech. **55**(1), 37–55 (2015)
65. R. Zhou, Z. Song, Y. Lu, 3D mesoscale finite element modelling of concrete. Comput. Struct. **192**, 96–113 (2017)
66. X. Zhou, H. Hao, Mesoscale modelling of concrete tensile failure mechanism at high strain rates. Comput. Struct. **86**(21–22), 2013–2026 (2008)